The effect of a mainshock on the size distribution of the aftershocks

Gulia L.[1*], A.P. Rinaldi[1], T. Tormann[1], G. Vannucci[2], B. Enescu[3] and S. Wiemer[1]

[1] Swiss Seismological Service, ETH Zurich, Switzerland.
[2] Istituto Nazionale di Geofisica e Vulcanologia, Bologna, Italy.
[3] Department of Geophysics, Kyoto University, Kyoto, Japan.

L. Gulia: Laura Gulia (lgulia@ethz.ch)
A. P. Rinaldi: Antonio Pio Rinaldi (antoniopio.rinaldi@sed.ethz.ch)
T. Tormann: Thessa Tormann (thessa@sed.ethz.ch)
G. Vannucci: Gianfranco Vannucci (gianfranco.vannucci@ingv.it)
B. Enescu: Bogdan Enescu (benescu@kugi.kyoto-u.ac.jp)
S. Wiemer: Stefan Wiemer (stefan.wiemer@sed.ethz.ch)

Keypoints

1. We develop a stacking approach to *b*-value time-series centered on the mainshock time in order to extract the generic behavior.
2. Applying this approach to well-recorded aftershock sequences, we demonstrate that the *b*-value increase by 20-30% after a mainshock.
3. We develop a Coulomb stress-based model explaining the post-mainshock b-value increase and propose an empirical relationship to be used to forecast aftershock hazard.

Keywords: *b*-value, aftershocks, stacking, Reid theory, differential stress, earthquake hazard forecasting.

Abstract

A systematic decay of the aftershock rate over time is one of the most fundamental empirical laws in Earth science. However, the equally fundamental effect of a mainshock on the size distribution of subsequent earthquakes has still not been quantified today and is therefore not used in earthquake hazard assessment. We apply a stacking approach to well-recorded earthquake sequences to extract this effect. Immediately after a mainshock, the mean size distribution of events, or *b*-value, increases by 20-30%, considerably decreasing the chance of subsequent larger events. This increase is strongest in the immediate vicinity of the mainshock, decreasing rapidly with distance but only gradually over time. We present a model that explains these observations as a consequence of the stress changes in the surrounding area caused by the mainshocks slip. Our results have substantial implications for how seismic risk during earthquake sequences is assessed.

1. Introduction

Earthquakes interact with each other by changing the state of stress in their surroundings (Stein, 1999). The static and dynamic stress changes caused by their instantaneous displacement decay with growing distance from the fault (Okada, 1992). The most noticeable consequence of this stress change is a dramatic increase in the seismicity rate (Ebel et al., 2000). The aftershock phenomenon is one of the most intensely studied properties of such events. Based on empirical observations of the 1891 Nobi earthquake, Omori (1895) described how aftershock activity decreased by K/(t+c), where K and c are constants that describe aftershock productivity and delay time (Utsu et al., 1995). Utsu (1961) defined the so-called modified Omori Formula, observing that aftershock sequences decay with different exponents. Alternatives to the Omori law have also been proposed (Mignan, 2015, 2016). Today, aftershock activity is typically described as part of a cascading or branching process, and the Epidemic Type Aftershock Sequence (ETAS; Ogata, 1988, 1998) Model is the best currently available statistical description of seismicity (Marzocchi et al., 2017). There is also a good physics-based understanding, often derived from laboratory friction experiments (Toda et al., 2005), of how stress changes cause the seismicity rate to increase in some regions by a factor of 1,000 or more, whereas, in other regions, Coulomb stress changes induced by a mainshock may be negative, lowering the earthquake rate (Wyss and Wiemer, 2000; Gerstenberger et al., 2005).

However, changes in stress, should not only impact earthquake activity rate, but also the frequency-size, or frequency-magnitude, distribution (FMD) of the subsequent earthquakes. The FMD is typically described using another fundamental empirical law of seismology, the 'Gutenberg-Richter relationship' (Gutenberg and Richter, 1944), which estimates the number of earthquakes N larger than or equal to magnitude M, via the formula $\log(N) = a\text{-}bM$, whereby the a-value is a volume productivity measure and the b-value quantifies the FMD slope: a lower b-value describes a distribution with a higher proportion of larger magnitudes, and vice versa. Repeated laboratory measurements (Scholz, 1968; Amitrano et al., 2003; Goebel et al., 2013) have established that the applied differential stress to a rock sample determines the b-value: the higher the applied differential stress, the lower the b-value. Observations from various tectonic contexts are consistent with this inverse proportionality of b on differential stress (Schorlemmer et al., 2005), indicating for example b-values' systematic dependency on faulting style (Gulia & Wiemer, 2010), depth (Spada et al., 2013) and fluid pressure (Bachmann et al., 2012).

To date, the effect of a mainshock's differential stress change on the subsequent seismicity has not been systematically investigated, but individual case studies suggest that sometimes higher b-values are observed after a mainshock (Wiemer & Katsumata, 1999; Wiemer et al.,

2002; Tormann et al., 2012, 2014, 2015; Ogata & Katsura, 2014; Tamaribuchi et al., 2018). These individual observations highlight the important question of whether such high post-mainshock *b*-values are characteristic of aftershock sequences and, if so, whether, when, or how they recover. Here, for the first time, we use a stacking approach to *b*-value time-series to enhance the signal-to-noise ratio of their changes, allowing us to extract the generic behavior previously masked by random variations and systematic biases.

2. Data and Method

Transients in *b*-value are difficult to establish with confidence, since temporal variation can easily be mimicked or masked by spatial activation changes (Wiemer et al., 2002; Tormann et al., 2013), especially when the completeness of recording changes dramatically over time (Wiemer & Wyss, 2002). Consequently, any robust analysis of transients necessitates meticulous sequence-specific data selection systematically applied so as not to introduce any biases into the analysis.

We defined a fast, homogeneous, objective and reproducible methodology to select the region for analysis based on the mainshock's focal mechanism (FM). FMs provide all required information (strike, dip, rake) to model a first-order rectangular fault plane. By deriving a tectonic fault-style (Frohlich, 1992) and by applying empirical formulas (Wells and Coppersmith, 1994), source dimensions and relative uncertainties can be derived directly from the mainshock magnitude (Figure 1). Between the two available nodal planes, we consider the one with the highest number of immediate aftershocks (hereinafter we refer to the chosen fault plane as the *box*).

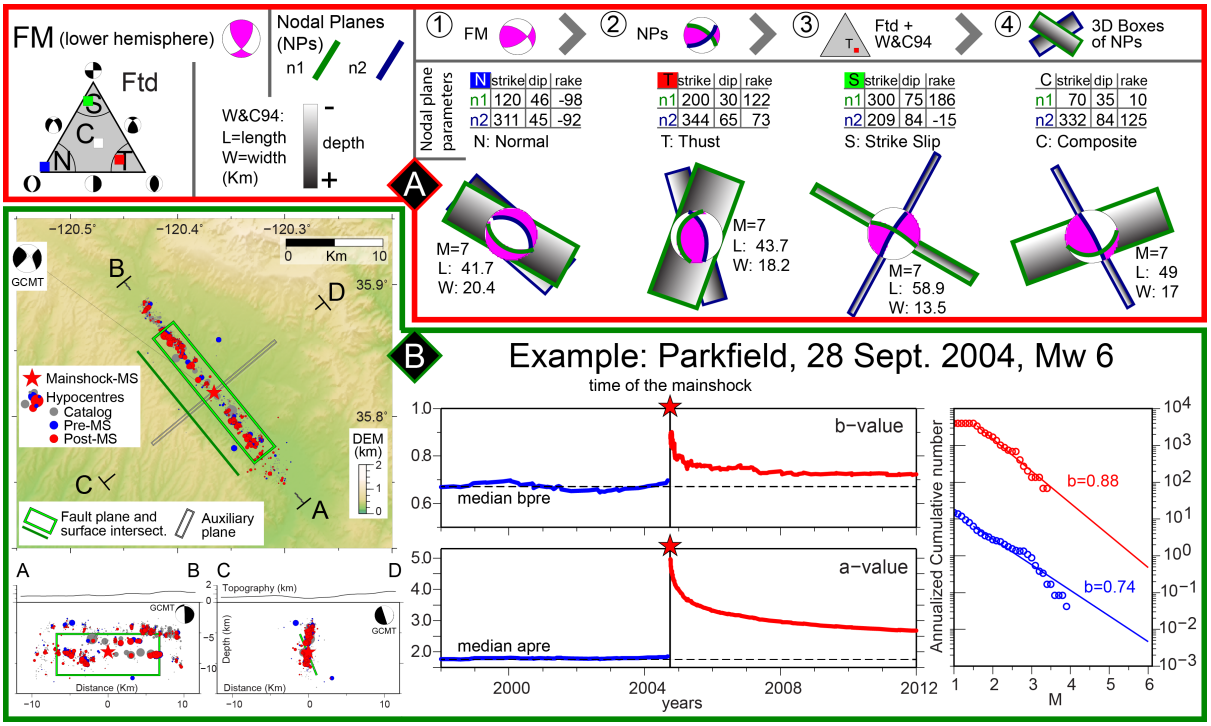

Figure 1: *Upper panel-red frame: Schematic workflow: from the FM to the fault planes and an example of the inferred geometry for a M7 earthquake in different tectonic styles. High panel (A)-red frame: method details about the 4 steps to constrain the geometry of the box: from FM (n.1) (lower hemisphere, in violet) to nodal*

planes (NPs in green and blue colours, n.2). By plotting the nodal planes parameters (strike, dip, rake) in a Frohlich (1992) triangular diagram (Ftd, n.3) we deduce the tectonic style (N=normal, T=thrust, S=strike-slip, C=composite) and we infer the plane dimensions (length –L- and width –W) as function of the magnitude (M) and of the empirical formulas of Wells and Coppersmith (W&C, 1994). The geometry of the nodal planes (dip direction in shades of grey) and their dimensions constrain the seismogenic boxes (n.4). Four examples for FMs with M=7 and different tectonic styles are reported to display the planes that individuate the fault plane and the auxiliary one. Lower panel (B)- green frame. On the left (map): seismicity data plot: mainshock (red star); earthquakes below the magnitude of completeness (grey); background (blue); aftershocks (red). The fault plane (green) is also represented in longitudinal (A-B) and transversal (C-D) sections with respect to the strike. On the right, an example: a-value and b-value time-series and FMD for the background (blue) and the first b-value estimated after the mainshock (red) for Parkfield, 2004

We processed all magnitude 6.0 or larger independent (i.e. not themselves aftershocks, according to Gardner & Knophoff, 1974), events available to us in the high-quality catalogs (i.e. local catalogs with a low magnitude of completeness) covering California (ANSS), Japan (JMA), Italy (Gasperini et al., 2013) and Alaska (AEIC), giving us 58 sequences in all: 20 in California, 35 in Japan, 2 in Italy and 1 in Alaska. For each of these mainshocks, we construct a box based on the FM parameters (Figure 1). In order to quickly and homogeneously compare worldwide sequences, all the boxes were derived using mechanisms from the Global Centroid Moment Tensor database (GCMT, Dziewonski et al., 1981; Ekström et al., 2012), whereas we performed the temporal parameter analysis based on the local catalogs, taking advantage of lower completeness magnitudes and higher location accuracy. Although the GCMT also provides coordinates of the FM centroid, we placed the box at the hypocentre listed in the corresponding local catalog. Sometimes the offset between those two locations can be significant (tens of kilometres) because centroids are poorly constrained by the Moment Tensor inversion procedure (Smith & Ekström, 1997; Kagan, 2003) and are thus unreliable in many cases. This choice can result in asymmetric distributions of the events with respect to their hypocentre for sources with strong directivity and asymmetric fault rupture. To acknowledge variation in the spatial spread of aftershocks between different sequences, we estimate the density of events (immediate aftershocks, e.g. during the first days) calculating the ratio between the number of events at increasing distances from the box -from 3 to 10 km, in all the 3D directions- and the fault length. We then choose the distance that yields the highest aftershock density (i.e. the highest ratio). 3 and 10 km represents, respectively, the uncertainty in the fault size estimation for a M6 and for a M7 due to the magnitude conversion and homogenization process (e.g. in the Italian catalog, Gasperini et al., 2013). Within this distance from the box, we select all events in the local catalog.

2.1 The individual time-series

To compute parameters, we choose a constant number of events approach, moving the window through the catalog event by event, and plotting the data at the end of the considered time interval (Tormann et al., 2013). Computing the *b*-values critically depends on the correct estimate of the magnitude of completeness (Mc; Wiemer & Wyss, 2000; Woessner & Wiemer, 2005; Mignan & Woessner, 2012) which is known to vary over time and changes especially strongly after large earthquakes (Wiemer & Katsumata, 1999). To avoid overly conservative estimates at times when smaller events were recorded properly, we estimate the Mc for each time interval and apply a four-level-approach: we first estimate the overall

completeness based on the maximum curvature method (Wiemer and Wyss, 2000) of the pre-mainshock catalog as well as the second half of the Gardner and Knopoff (1974) aftershock time window (when incompleteness that affects the first phase of the aftershock process is not considered problematic any more), assuming this to be the best Mc level for this region, and use the maximum of those two as the pre-cutting level. We then estimate for each time window Mc via maximum curvature plus 0.2 (Wiemer & Wyss, 2000; Woessner & Wiemer, 2005) to reach the dataset from which we estimate the *a*- and *b*-values if more than 50 events, above the Mc, are available.
To account in addition for the short-term aftershock incompleteness (Kagan, 2004) we removed any events that occurred after the mainshock until the Mc calculated by using the mainshock-magnitude dependent Mc estimate proposed by Helmstetter et al. (2006) matched the pre-cutting level.

We adopt a window length of 150 for the events preceding the mainshock and 400 for events following the mainshock, due to their different abundances. The *b*-value was calculated using the maximum likelihood method. For most earthquake sequences, numerous aftershocks are observed within the box, but there is only very sparse background seismicity before the mainshock, too little to estimate an event specific *b*-value. In those cases, we estimate a regional background *b*-value, selecting the closest 300 events that occurred before the mainshock and using this dataset to compute the local reference *b*-value. In such cases, the *b*-values preceding the mainshocks are not represented by a time-series but by a single point preceding the mainshock.

To assess the linearity of each FMD, we adopt the non-linearity index (NLI; Tormann et al., 2014): this algorithm judges the linearity of a sample catalog based on the *b*-value estimates for different cut-off magnitudes, starting at Mc and increasing up to the highest magnitude above which 50 events are still observed. The NLI index is the ratio of the standard deviation of these *b*-value estimates divided by the largest individual uncertainty (Shi and Bolt, 1982) in the single *b*-value estimates, if at least 5 *b*-value estimates can be calculated. If NLI>=1, the FMD is considered linear. The overall approach is summarised in Figure 1 for the example of the M6. Parkfield (California) mainshock that occurred on 28 September 2004: the time-series of *a*-values reveals an increase in aftershock activity of roughly a factor of 1,000, which decreases exponentially over time. The *b*-values increases by about 20%, from about 0.74 to 0.88, then gradually decrease over time. The respective FMDs are shown, too. In total, we can define the parameters of interest for 31 sequences out of 58 (15 in California, 14 in Japan, 1 in Italy and 1 in Alaska).

Once the individual time-series has been estimated, we normalise it by taking the median value of all the pre-mainshock estimates. Then, for each time step (i.e. one day), we calculate the percentage differences from the reference level (100%). This allows us to stack the individual time-series even though the absolute *b*-values vary due to different tectonic regimes, magnitude scales and other factors. Since we are interested in solving potential systematic changes in the parameters before and after the mainshock, we also shifted the time of the mainshock to zero for each sequence and interpolated the derived parameters on a daily

scale for the sequence-specific catalog length before and after the mainshock. Finally, we stacked all the 31 sequences: for each day we calculate the mean of the estimates for the individual sequences to derive the general behavior. We establish the uncertainty around the mean by a bootstrap technique over a paradata set of 10 times the number of sequences (i.e. 310).

3. Results

In Figures 2A-D, we show the results of the time-shifted, normalised, stacked time-series, revealing a trend: immediately after the mainshock, the *b*-value increases by about 20% (Figure 2A), a jump that is statistically significant and lies outside the observed pre-mainshock variability of the stacked time-series. The peak increase in the *b*-value occurs at between 1 and 2 months. The *b*-value subsequently remains high for the next 5 years, decreasing only gradually. Note also the 10% decrease in *b*-value during the months to days prior to the mainshock. While this anomaly is consistent with selected case studies and laboratory studies that have reported dropping precursory *b*-values (Papadopoulos et al., 2010; Tormann et al., 2015; Gulia et al., 2016) the number of pre-mainshock stacked time-series is only 8.

The stack of the *a*-value (Figure 2B) exhibits the well-known increase in activity by a factor of 1,000 after a mainshock, followed by exponential decay. We also show the Mc stack over time (Figure 2C) that indicates no systematic change in the Mc before and after the mainshock. The instantaneous *a*- and *b*-values can be used to directly compute the probability of an earthquake of any magnitude (Wiemer & Wyss, 1997; Gulia et al., 2016). Of special interest is the probability of a secondary event equal to or even larger than the mainshock itself. The curve of this normalised probability is plotted in Figure 2D. It shows an increase above the pre-mainshock background level by a factor of 10,000 immediately after the mainshock and then a gradual decrease. For comparison, we also compute the current best practice in aftershock hazard assessment, using a constant *b*-value (black line in Figure 2D): this probability exceeds the one computed with a temporally varying *b*-value by a factor of at least 10 for many years.

Next, we analyse the spatial extent of the *b*-value increase by stacking 3 different and independent sampling volumes around the mainshock fault volume (Figure 3E-J): the highest increase in both *b*- and *a*-values is observed in the volume limited to up to 2km away from the mainshock. Here, the *b*-values increase by 30% after the mainshock. Volumes between 2 and 15 km away from the mainshock also have higher *b*-values, up by about 20% and provide an enticing hint that *b*-values in this distance range tend to increase during the months prior to the mainshock, a trend opposite to the precursory decrease observed in the immediate vicinity of the quake. In volumes from 15 to 25 km away, the *b*-values increase by only about 5% after the mainshock, while *a*-values rise much more sharply, indicating that not only the temporal recovery but also the two spatial footprint changes appear to be different.

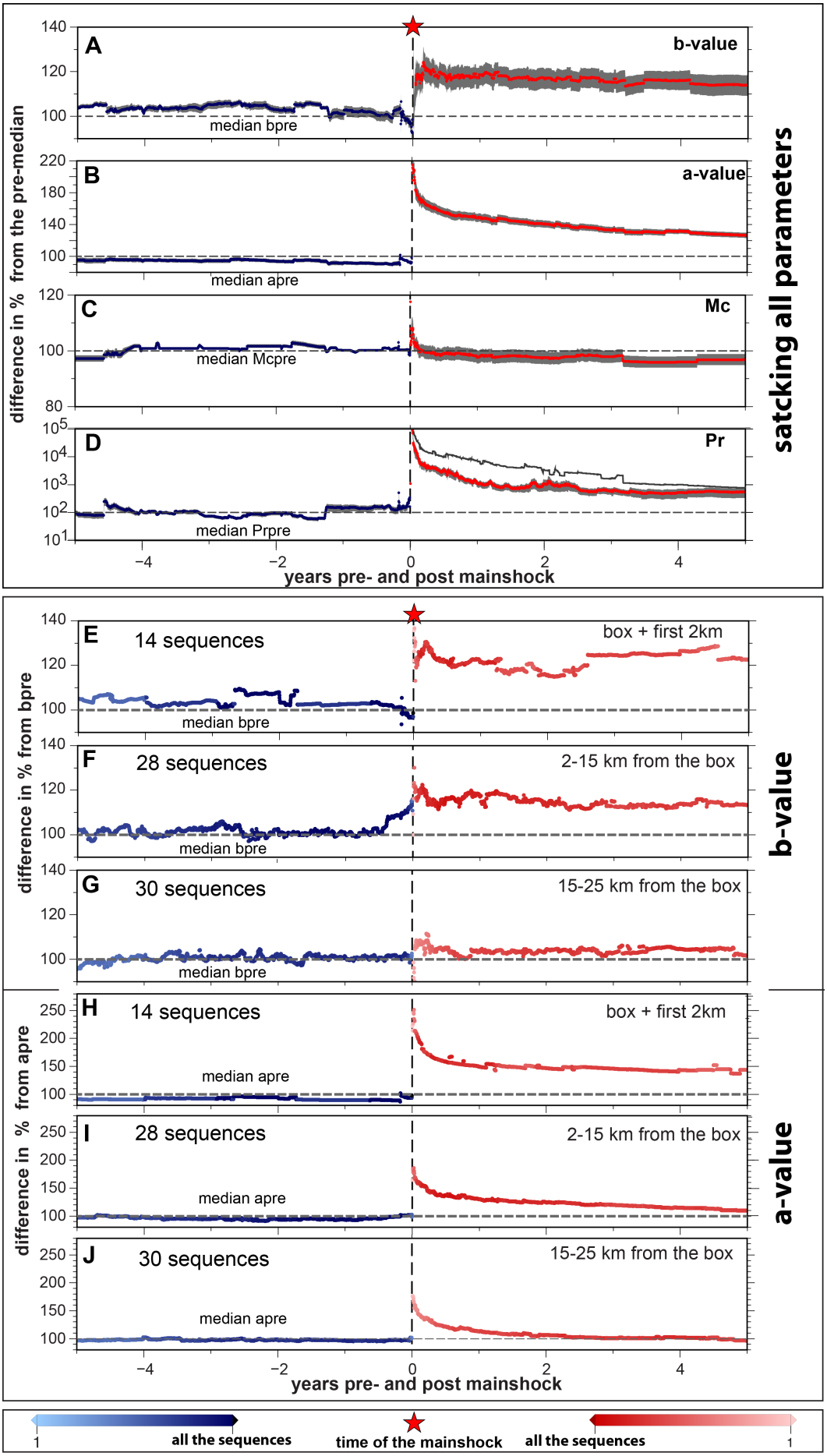
A
b-value
median bpre
B
a-value
median apre
C
Mc
median Mcpre
D
Pr
median Prpre
difference in % from the pre-median
satcking all parameters
years pre- and post mainshock
E
14 sequences
box + first 2km
median bpre
F
28 sequences
2-15 km from the box
median bpre
G
30 sequences
15-25 km from the box
median bpre
difference in % from bpre
b-value
H
14 sequences
box + first 2km
median apre
I
28 sequences
2-15 km from the box
median apre
J
30 sequences
15-25 km from the box
median apre
difference in % from apre
a-value
years pre- and post mainshock
all the sequences
time of the mainshock
all the sequences

246

Figure 2: *A-D): Stacking the parameters of interest for the 31 sequences showing the difference in percentage to the reference value. Blue curves indicate daily values over the 5 years preceding the mainshock. Red curves chart the same values over the first subsequent 5-year period. A) b-value; B) a-value; C) magnitude of completeness; D) daily probability for an event with magnitude greater or equal to the mainshock, calculated from the values in the subplots A-B (Pr). In black, the same probability estimated using the background constant b-value. Grey indicates the uncertainty by bootstrap. E-J: Stacking b-values (E-G) and a-values (H-J) as a function of the distance, re-sampling the sub-catalog and estimating a- and b-values for the events inside three different volumes. The shaded colors (red and blue) represent the number of sequences that have an estimation.*

4. Modeling the changes in aftershocks distribution

The occurrence of an earthquake affects the stress distribution in the area surrounding the fault zone. For each point of a 3D domain, the stress changes caused by a mainshock can be computed using analytical solutions for a dislocation in an elastic half-space (Okada, 1992). Such computation provides the full stress tensor at each evaluation point, making it then straightforward to derive variables such as the differential stress changes and the Coulomb Failure Stress (CFS).

On the one hand, the variation in differential stress can be computed assuming an initial state (dependent on the faulting style and resulting in a $\Delta\sigma_{ini} = \sigma_1 - \sigma_3$) and recalculating the principal stress by solving for the eigenvalues in the final configuration (i.e. after summing the changes computed by the Okada model). Then, the differential stress change in percentage is:

$$\delta\Delta\sigma = \left(\Delta\sigma_{fin} - \Delta\sigma_{ini}\right)/\Delta\sigma_{ini}$$

the values of the initial principal stresses are chosen such that $\Delta\sigma_{ini}$ is 66, 133, 199 MPa for normal, strike-slip, and thrust faulting respectively. These values are calculated assuming that one of the three principle stresses is always the lithostatic and vertical at a Seismogenic depth of 9 km with rock density 2500 kg/m3. The maximum and minimum principal stresses to calculate the differential stress for the respective cases (normal, strike-slip, and thrust) are then calculated using ratio with respect to the vertical stress. On the other hand, computing changes in Coulomb Failure Stress (CFS) provides a first-order understanding of where future aftershocks are likely to occur (Stein, 1999). We can calculate a scaled changes in CFS as:

$$\delta\Delta CFS = \left(\Delta\tau + \mu(\Delta\sigma_n + B\sigma_m)\right)/\Delta\sigma_{ini}$$

in which $\Delta\tau$ is shear stress and $\Delta\sigma_n$ is the normal stress. μ is the frictional coefficient with a value of 0.6, with σ_m being the mean effective stress and B = 0.5 the Skempton's coefficient. We consider an elastic medium with a Young's modulus of 30 GPa and a Poisson's ratio of 0.3. The calculated variation for both stress and CFS are dependent on the assumed focal mechanism, and we assume that both source and receivers have the same orientation, with a strike of roughly 30˚ and a dip of 90˚ for the strike-slip faults, and fault dipping ~60˚ for normal faults and ~30˚ for thrusts, with both cases having strike of 0˚. Such angles represent the optimal orientation if the principal stresses are oriented along coordinate axes.

In order to have an understanding of the stress variation in three dimension, we calculate the

mean spatial variation of both $\delta\Delta\sigma$ and $\delta\Delta CFS$ for regions at varying distances from the fault in 1 km steps (e.g. the value at 3 km accounts for values at the receiver between 2 and 3 km). To avoid singular values, we always exclude values in the first 0.5 km.

Figures 3A and 3C show an example of the expected variation in space for an optimally oriented fault reactivating in a Mw=7 mainshock, with dimensions based on empirical relationship (Wells & Coppersmith, 1994) and top of the fault at 7 km depth. The areas near the fault plane are subjected to a decrease in differential stress or an average larger value of CFS, which correlates with the observed increase in *b*-value.

To analyze this effect as a function of magnitude, we take the average value of relative stress changes within the first 5 km. Figures 3B and 3D shows the variation of average CFS and differential stress changes as a function of magnitude, with percentage variation being proportional (inversely proportional) to the average value of positive Coulomb (differential stress). The model predicts a change of about 8% for CFS and 3% for differential stress at a distance of 5 km for the case of normal faults with magnitude $M_w = 8$.

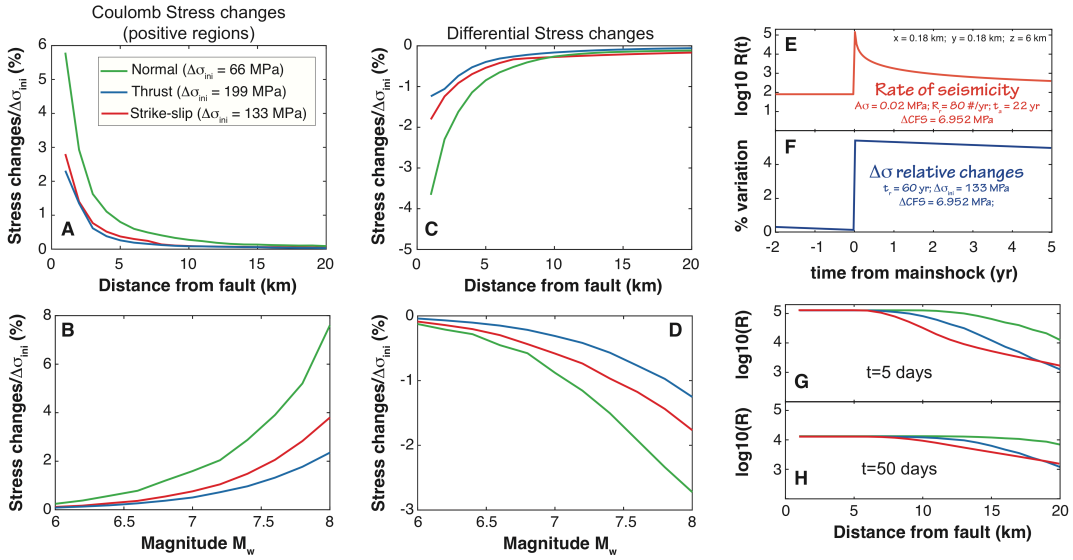

Figure 3: *A-B: percentage variation of positive Coulomb Failure Stress changes as function of distance (A) and magnitude (B for the 3 different stye of faulting; C-D: percentage variation of differential stress changes as function of distance (C) and magnitude (D). E-F: expected temporal evolution of the seismicity rates (D) and of stress changes recovery (F). G-H: earthquake productivity as function of distance for 5 days (G) and 50 days (H) after mainshock for 3 different style-of-faulting.*

While Figures 3A-D refer to co-seismic variation, we can use a well-established constitutive law for earthquake production and a classical elastic rebound theory for the stress to extrapolate the temporal variation of the changes in the seismicity rate and percentage variation of differential stress.

The temporal evolution of the earthquake productivity is calculated by assuming rate-and-state friction (Dieterich et al., 2000) according to the formula:

$$\frac{\mathrm{R}}{r} = \left[\left(e^{-\Delta S/A\sigma_{n,0}} - 1\right)e^{-t/t_a} + 1\right]^{-1}$$

where R is the expected rate of aftershocks at time t, r is the background rate of seismicity and t_a is the aftershock decay time A is a constant value, and $\sigma_{n,0}$ is the value of the normal effective stress. ΔS is an equivalent Coulomb stress, defined as:

$$\Delta S = \Delta\tau + \left(\frac{\tau_0}{\sigma_{n,0}} - \alpha\right)(\Delta\sigma_n + p)$$

We use an equivalent friction $\mu = \tau_0/\sigma_{n,0} - \alpha = 0.3$ and the value of $A\sigma_{n,0}$ depends on the faulting style (0.0116 MPa, 0.0214 MPa, and 0.02 MPa, for normal, thrust, and strike-slip, respectively – Heimisson & Segall, 2018). The temporal evolution of differential stress is simply calculated by assuming linear elastic rebound theory: coseismic slip is completely recovered with a given recurrence time.

Figures 3E-F show the expected temporal evolution for a point located 1 km above the fault zone along dip. The seismicity rate increases up to 10^5 earthquakes/years and decreases exponentially over time to a value slightly above the background level (80 events per year) after five years (Figure 3E). If the stress recovery is elastic, and assuming for example an arbitrarily selected 60-years recurrence period, the CFS for example recovers linearly with little change over the first 5 years, remaining at about 5% above the regional value (Figure 3F). A similar trend could be extrapolated for the differential stress, although with negative average value in the considered domain. The chosen recurrence period was assumed quite short to illustrate that even in a case of unusually fast recovery, in a five years' timeframe the stresses are still far from the background value (if assuming elastic response only).

Similar to stress change, the spatial distribution and amplitude of earthquake productivity depend on the fault's orientation and faulting style. A comparison of the results in Figure 3G and 3A/C shows that for the three different faulting styles we expect differences in seismicity and relative stress changes, with normal faults being the most receptive, but the general trends persist. While the rate of aftershocks strongly increased up to 10 km away from the fault (depending on the tectonic style), the stress changes are largely confined to an area within the first 5 km from the fault.

Summing up, our simple model shown in Figure 3 suggest that areas of positive CFS (or average negative differential stress) exist after a mainshock, which would explain the observed increased *b*-value. Assuming this correlation does exist, the amplitude of the *b*-value increase should depend systematically on magnitude and faulting style. According to the model, the *b*-value should recover slower and linearly with time, rather than decaying exponentially, as observed for aftershock rates. The *b*-value increase should be confined to the immediate vicinity of the mainshocks.

Inspired by these model's predictions, we now re-examine our stacking results. We currently lack the resolution power necessary to analyse quantitatively the spatial correlation of *b*-value

365 increase with areas of positive CFS (or negative differential stress), and we also have too
366 limited focal mechanism diversity for a meaningful analysis. We first analyze the long-term
367 trend: in Figures 4A-B, we extend the stacks to 15 years after a mainshock occurrence and
368 indeed find the recovery in *b*-value to be very different from the change in *a*-values. The rate
369 increase decays exponentially with time, as expected and in accordance with the Omori's
370 law. After 15 years it almost reached the pre-event background level. In contrast, the *b*-values
371 remain high through time, decreasing only slightly, in agreement with our theory.
372
373 To investigate magnitude dependence, we compute stacks of the *b*-values for events above
374 and below magnitude 7.0 (Figures 4C-D). These confirm that events with magnitude equal or
375 bigger than 7 experience an increase approaching 40%, while smaller mainshocks cause an
376 increase of about 20%. Conversely, the *a*-value increase (Figure 4E-F) appears rather
377 independent of magnitude. The magnitude dependence of *b*-value increase would be even
378 further pronounced if stress drop depended on magnitude. Although it is often assumed that
379 stress drop is independent of magnitude, for large strike slip earthquakes is was pointed out
380 that slip increases with rupture length (Scholz, 1982), which has been confirmed more
381 recently (Hanks and Bakun, 2002; 2008). Because these earthquakes all have the same width,
382 constrained by the seismogenic thickness, then stress drop must increase by rupture length
383 and magnitude.
384
385 We also study the distance decay kernels in greater detail in Figures 4G-H and find they tally
386 with the theoretical prediction that *b*-values increase is confined to the immediate vicinity of
387 the fault, decaying rapidly with distance, whereas *a*-value increases decay more gradually
388 with distance from the fault. Our more detailed analysis has therefore shown good agreement
389 between model prediction and data.
390

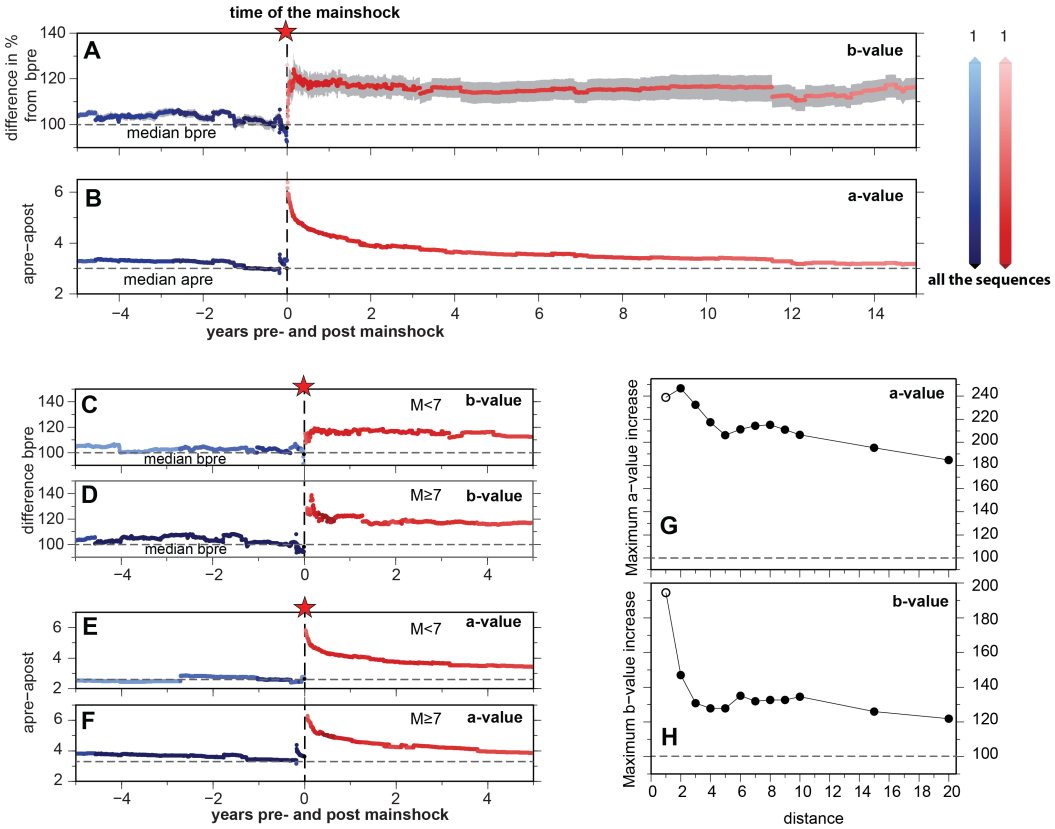

Figure 4: A-B: a-value and *b*-value stacking showing the difference in percentage from the reference value. C-D: *b*-value stacking and a-value time-series for the 20 sequences with mainshock M<7 and for the 11 sequences with mainshock M>=7. G-H: percentage of the maximum *a*-value (g) and *b*-value (h) increase as a function of the distance from the box (km) over the first 3 months of aftershocks.

5. **Discussion and Conclusions**

By using stacking of *b*-value time-series as a tool to enhance the signal-to-noise ratio, our study is the first to quantify the general impact of a mainshock on the size distribution of subsequent earthquakes. The stacked signal of an increase in b-value by 20 – 30% after a mainshock is very clear and highly significant (Figure 2). We document for the first time the space, time, faulting style and magnitude dependency of the *b*-values change, and establish that the *b*-value change transients behave distinctly different from the ones of aftershock rate change, described Omori's law. The differential stress change of the mainshock is a highly plausible mechanism explaining the empirical observations and is fully consistent with laboratory measurements of the *b*-value dependence on stress.

We propose that the changes in *b*-value as a function of time after a mainshock can be described using the formula:

$$b_{post} = b_{pre} (1 + d (1 - t/Rt))$$

where *Rt* is the return period of the mainshock and *d* is a constant that may depend on the magnitude of the mainshock, the faulting style and possible tectonic region. A default value for *d*, as observed in Figure 2A, would be 0.2. The observed long-lasting increase on the *b*-values matches the fault's loading rate.

Our results address one of the open issues regarding Coulomb stress changes and elastic rebound theory by Reid (1911). Elastic rebound theory predicts that after a mainshock, it will take time to recover the strain released in the mainshock, so the subsequent years should be the least hazardous. On the other hand, Coulomb stress change models and operational aftershock forecasting models such as ETAS (Ogata, 1988, 1998) or STEP (Gerstenberger, et al., 2005) predict the highest rate of re-rupturing on the same fault immediately after the mainshock. These models forecast an unrealistically high chance for a repeat of the mainshock rupture (Figures 2D) and thus substantially overestimate aftershock hazard. So far, operational earthquake forecasting models have – on a somewhat ad-hoc basis - lowered the maximum magnitude or removed this mainshock fault from their computations (Field et al., 2017). Our results suggest that this paradox is resolved when considering the stress changes and their impact on the earthquake size distribution. While numerous small events occur near the mainshock fault, larger ones are far rarer than existing models predict. Indeed, Figure 4H suggests that the *b*-values right on the fault plane increase by much more than 120%, consistent with observations from individual sequences showing that the strongest *b*-value change occurs near the patches of the largest slip (Tormann et al., 2015).

CFS analysis after significant earthquakes has been frequently conducted after large mainshocks, with hundreds of studies conducted since the ground-breaking work done on the Landers earthquake (King et al., 1994). The performance assessment of these aftershock forecasts has been mixed (Hardebeck,1998; Nandan et al., 2016). Based on our modeling (Figure 3) we postulate that in the future such studies should not only consider the effect of

CFS on earthquake rates, but also the absolute value of the change in stress and its impact on earthquake size distribution if they are to forecast earthquake hazard accurately.

We conclude by suggesting that stacking carefully selected, time-shifted and normalised time-series of *b*-values has proven to be a powerful approach for gaining insights into physical processes. Our analysis has also shown hints of precursory signals that are consistent with pre-slip on the fault: decreasing *b*-values in the immediate vicinity of the fault, and increasing ones nearby (Figures 2E-F). Future studies covering more events may be able to resolve these important precursory changes using the stacking approach introduced here.

449 **References**

450 Amitrano, D. (2003), Brittle-ductile transition and associated seismicity: Experimental and
451 numerical studies and relationship with the b value. *J. Geophys. Res.* 108**,** 1–15.

452 Bachmann, C. E., S. Wiemer, B. P Goertz-Allmann,. & J. Woessner (2012), Influence of
453 pore-pressure on the event-size distribution of induced earthquakes. *Geophys. Res. Lett.* ,39,.
454 L09302, doi:10.1029/2012GL051480.

455 Dieterich, J. H., V. Cayol & P.G. Okubo (2000), The use of earthquake rate changes as a
456 stress meter at Kilauea volcano. *Nature,* 408, 457–460.

457 Dziewonski, A. M., T.A. Chou & J.H. Woodhouse (1981), Determination of earthquake
458 source parameters from waveform data for studies of global and regional seismicity. *J.*
459 *Geophys. Reasearh,* 86**,** 2825–2852.

460 Ebel, J. E., K.-P Bonjer & M. C. Oncescu (2000), Paleoseismicity: Seismicity evidence for
461 past large earthquakes. *Seismol. Res. Lett.,* 71, 283–294.

462 Ekström, G., M. Nettles & A. M. Dziewoński (2012), The global CMT project 2004-2010:
463 Centroid-moment tensors for 13,017 earthquakes. *Phys. Earth Planet. Inter.,* 200–201**,** 1–9.

464 Enescu, B., J. Mori, M. Miyazawa &.Y. Kano (2009), Omori-Utsu law c-values associated
465 with recent moderate earthquakes in Japan. *Bull. Seismol. Soc. Am.,* 99**,** 884–891.

466 Field, E. H. *et al.* (2017), A Synoptic View of the Third Uniform California Earthquake
467 Rupture Forecast (UCERF3). *Seismol. Res. Lett.,* 88**,** 1259–1267.

468 Freed, A. M. (2007), Afterslip (and only afterslip) following the 2004 Parkfield, California,
469 earthquake, *Geophys. Res. Lett.,* 34(6), doi:10.1029/2006gl029155.

470 Frohlich, C. (1992), Triangle diagrams: ternary graphs to display similarity and diversity of
471 earthquake focal mechanisms. *Phys. Earth Planet. Inter.* 75, 193–198.

472 Gardner, J. K. & L. Knopoff (1974), Is the Sequence of Earthquake in Southern California,
473 with Aftershockes Removed. Poissonian? *Bull. Seismol. Soc. Am.* 66, 1271–1302.

474 Gasperini, P., B. Lolli & G. Vannucci (2013), Empirical calibration of local magnitude data
475 sets versus moment magnitude in Italy. *Bull. Seismol. Soc. Am.* 103, 2227–2246.

476 Gerstenberger, M. C., S. Wiemer, L. M. Jones & P.A. Reasenberg (2005), Real-time
477 forecasts of tomorrow's earthquakes in California. *Nature,* 435, 328–331.

478 Goebel, T. H. W., D. Schorlemmer,, T. W. Becker, G. Dresen & C. G. Sammis (2013),
479 Acoustic emissions document stress changes over many seismic cycles in stick-slip
480 experiments. *Geophys. Res. Lett.,* 40**,** 2049–2054.

481 Gulia, L. & S. Wiemer (2010), The influence of tectonic regimes on the earthquake size
482 distribution: A case study for Italy. *Geophys. Res. Lett.,* 37, L10305,
483 doi:10.1029/2010GL043066.

484 Gulia, L., T. Tormann, S., Wiemer,, M. Herrmann & S. Seif (2016), Short-term probabilistic
485 earthquake risk assessment considering time-dependent b values. *Geophys. Res. Lett.,* 43,
486 1100–1108, doi:10.1002/2015GL066686.

487 Gutenberg, B. & C. F. Richter (1944), Frequency of earthquakes in California. *Bull.*
488 *Seismol. Soc. Am.,* 34, 185–188.

489 Hanks, T. C. & W. H. Bakun (2002), A bilinear source-scaling model for M-log A
490 observations of continental earthquakes. *Bull. Seismol. Soc. Am.*, 92(5), 1841-1846,
491 doi:10.1785/0120010148.

492 Hanks, T. C., and W. H. Bakun (2008), M-log A observations for recent large earthquakes.
493 *Bull. Seismol. Soc. Am.*, 98(1), 490-494, doi:10.1785/0120070174.

494 Hardebeck, J. L., J. J. Nazareth & E. Hauksson (1998), The static stress change triggering
495 model: Constraints from two southern California aftershock sequences, *J. Geophys. Res.*,
496 **103**(B10), 24427–24437.

497 Heimisson, E. R. & P. Segall (2018), Constitutive Law for Earthquake Production Based on
498 Rate-and-State Friction: Dieterich 1994 Revisited. *J. Geophys. Res. Solid Earth*,
499 doi:10.1029/2018JB015656

500 Helmstetter, A, Y. Y. Kagan & D. D. Jackson (2006), Comparison of Short-Term and Time-
501 Independent Earthquake Forecast Models for Southern California. *Bull. Seismol. Soc. Am.,*
502 96, 90–106.

503 Kagan, Y. Y. (2003), Accuracy of modern global earthquake catalogs. *Phys. Earth Planet.*
504 *Inter.,* 135, 173–209.

505 Kagan, Y. Y. (2004), Short-term properties of earthquake catalogs and models of earthquake
506 source. *Bull. Seismol. Soc. Am.,* 94**,** 1207–1228.

507 King, G. C. P., R.S. Stein & J. Lin (1994), Static stress changes and the triggering of
508 earthquakes. *Bull. Seismol. Soc. Am.,*, 84(3), 935–953.

509 Marzocchi, W., M. Taroni & G. Falcone (2017), Earthquake forecasting during the complex
510 Amatrice-Norcia seismic sequence. *Sci. Adv.,* 3.

511 Mignan A. & J. Woessner (2012), *Estimating the magnitude of completeness for earthquake*
512 *catalogsCommunity Online Resource for Statistical Seismicity Analysis*, doi:10.5078/corssa-
513 00180805

514 Mignan, A. (2015), Modeling aftershocks as a stretched exponential relaxation. *Geophys.*
515 *Res. Lett.,* 42, 9726–9732.

516 Mignan A. (2016), Reply to 'Comment on "Revisiting the 1894 Omori Aftershock Dataset
517 with the Stretched Exponential Function" by A. Mignan' by S. Hainzl & A. Christophersen.
518 *Seism. Res. Lett.,* 87, 1134–1137.

519 Nandan, S., G. Ouillon, J. Woessner, D. Sornette & S. Wiemer (2016), Systematic
520 assessment of the static stress triggering hypothesis using interearthquake time statistics. J.
521 Geophys. Res. Solid Earth, 121, 1890–1909, doi:10.1002/2015JB012212.
522
523 Okada, Y. (1992), Internal deformation due to shear and tensile faults in a half-space. *Bull.*
524 *Seismol. Soc. Am.,* 82, 1018–1040.

525 Ogata, Y. (1988), Statistical Models for Earthquake Occurrences and Residual Analysis for
526 Point Processes. *J. Am. Stat. Assoc.,* 83, 9–27.

527 Ogata, Y. (1998), Space-time point-process models for earthquake occurrences. *Ann. Inst.*
528 *Stat. Math.,* 50, 379–402.

529 Ogata, Y. & K. Katsura (2014), Comparing foreshock characteristics and foreshock
530 forecasting in observed and simulated earthquake catalogs. *J. Geophys. Res. Solid Earth* **119,**
531 8457–8477.

532 Omori, F. (1895), On the aftershocks of earthquakes. *Journal of the College of Science,*
533 *Imperial University of Tokyo,* 7, 111–200.

534 Papadopoulos, G. A., M. Charalampakis, A. Fokaefs & G. Minadakis (2010), Strong
535 foreshock signal preceding the L'Aquila (Italy) earthquake (Mw 6.3) of 6 April 2009. *Nat.*
536 *Hazards Earth Syst. Sci.,* 10, 19–24.

537 Reid, H. F. (1911), The Elastic-Rebound Theory of Earthquakes. *Bull. Dep. Geol. Univ.*
538 *Calif. Publ.,* 6, 413–444.

539 Scholz, C. H. (1968), The frequency-magnitude relation of microfracturing in rock and its
540 relation to earthquakes. *Bull. Seismol. Soc. Am.,* 58, 399–415.

541 Scholz, C. H. (1982), Scaling laws for large earthquakes: Consequences for physical models.
542 Bull. Seismol. Soc. Am., 72, 1-14.

543 Schorlemmer, D., S. Wiemer & M. Wyss (2005), Variations in earthquake-size distribution
544 across different stress regimes. *Nature,* 437, 539–542.

545 Shi, Y. & B. Bolt (1982), The standard error of the magnitude-frequency b value. *Bull.*
546 *Seismol. Soc. Am*., 72, 1677–1687.

547 Smith, G. P. & G. Ekström (1997), Interpretation of earthquake epicenter and CMT centroid
548 locations, in terms of rupture length and direction. *Phys. Earth Planet. Inter.* 102, 123–132.

549 Spada, M., T. Tormann, S. Wiemer & B. Enescu (2013), Generic dependence of the
550 frequency-size distribution of earthquakes on depth and its relation to the strength profile of
551 the crust. *Geophys. Res. Lett.,* 40, 709–714.

552 Stein, R. S. (1999), The role of stress transfer in earthquake occurrence. *Nature,* 402, 605–
553 609.

554 Tamaribuchi K. , Y. Yagi, B. Enescu B. & S. Hirano (2018), Characteristics of foreshock
555 activity inferred from the JMA earthquake catalog. *Earth, Planets Sp.,* 70–90,
556 doi:10.1186/s40623-018-0866-9

557 Toda, S., R. S. Stein,, K. Richards-Dinger & S. B. Bozkurt (2005), Forecasting the evolution
558 of seismicity in southern California: Animations built on earthquake stress transfer. *J.*
559 *Geophys. Res.,* 110, B05S16.

560 Tormann, T., S. Wiemer & J.L. Hardebeck (2012), Earthquake recurrence models fail when
561 earthquakes fail to reset the stress field. *Geophys. Res. Lett.,* 39, L18310,
562 doi:10.1029/2012GL052913 .

563 Tormann, T., S. Wiemer, S. Metzger,, A. Michael & J. L. Hardebeck (2013), Size distribution
564 of parkfield's microearthquakes reflects changes in surface creep rate. *Geophys. J. Int.,* 193,
565 1474–1478.

566 Tormann, T., S. Wiemer & A. Mignan (2014), Systematic survey of high-resolution b value
567 imaging along Californian faults: Inference on asperities. *Journal of Geophysical Research:*
568 *Solid Earth,* 119, 2029–2054.

569 Tormann, T., B. Enescu, J. Woessner & S. Wiemer (2015), Randomness of megathrust
570 earthquakes implied by rapid stress recovery after the Japan earthquake. *Nat. Geosci.,* 8, 152–
571 158.

572 Utsu, T. (1961), A statistical study on the occurrence of aftershocks. *Geophys. Mag.,* 30,
573 521–605.

574 Utsu, T., Y. Ogata, S, Ritsuko & Matsu'ura (1995),. The Centenary of the Omori Formula for
575 a Decay Law of Aftershock Activity. *J. Phys. Earth,* 43, 1–33.

576 Wells, D. L. & K. J. Coppersmith (1994), New Empirical Relationships among Magnitude,
577 Rupture Length, Rupture Width, Rupture Area, and Surface Displacement. *Bull. Seismol.*
578 *Soc. Am.,* 84, 974–1002.

579 Wiemer, S. & M. Wyss (1997), Mapping the frequency-magnitude distribution in asperities:

580 An improved technique to calculate recurrence times? *J. Geophys. Res.* 102, 15115.

581 Wiemer, S. & K. Katsumata (1999), Spatial variability of seismicity parameters in aftershock
582 zones. *J. Geophys. Res. Solid Earth,* 104, 13135–13151.

583 Wiemer, S. & M. Wyss (2000), Minimum magnitude of completeness in earthquake
584 catalogs: Examples from Alaska, the Western United States, and Japan. *Bull. Seismol. Soc.*
585 *Am.,* 90, 859–869.

586 Wiemer, S. & M. Wyss (2002), Mapping spatial variability of the frequency-magnitude
587 distribution of earthquakes. *Adv. Geophys.,* 45, 259-302 .

588 Wiemer, S., M. Gerstenberger & E. Hauksson (2002), Properties of the aftershock sequence
589 of the 1999 Mw 7.1 Hector Mine earthquake: Implications for aftershock hazard. *Bull.*
590 *Seismol. Soc. Am.,* 92, 1227–1240.

591 Woessner, J., S. Wiemer (2005), Assessing the quality of earthquake catalogs: Estimating the
592 magnitude of completeness and its uncertainty. *Bull. Seismol. Soc. Am.,* 95, 684–698.

593 Wyss, M. & S. Wiemer (2000), Change in the probability for earthquakes in southern
594 California due to the Landers magnitude 7.3 earthquake. *Science,* 290, 1334–1338.

595

596 **Acknowledgment**
597 Earthquake catalog data for California was obtained from the Advanced National Seismic
598 System (http://www.ncedc.org/anss/catalog-search.html). We thank JMA for sharing the
599 earthquake catalog. Data available from authors. Figures were produced with The Generic
600 Mapping Tools http://gmt.soest.hawaii.edu.
601
602 **Author Contribution**
603 L.G., T.T., S.W. conceived and developed the stacking analysis.
604 G.V. conceived and developed the FM part of the method and A.P.R. developed the
605 modeling.
606 L.G. led the design of the study and performed the data analysis.
607 L.G. and T.T. compiled the code.
608 L.G. performed Figures 1,2,4 (paper), figures 2, 3, 4 of the Supplementary material and the
609 Table; G.V. figure 1 (paper) and figure 1 of the Supplementary material; A.P.R. figure 3
610 (paper).
611 B.E. obtained the Japanese data sets used in the paper.
612 All authors participated in the discussion and interpretation of results and writing the
613 manuscript.
614
615 **Corresponding Author:** Laura Gulia (lgulia@ethz.ch)
616
617 **Author Information**
618 The authors declare no competing financial interests.